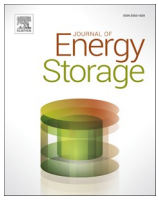
Journal of Energy Storage 157 (2026) 121636



Contents lists available at ScienceDirect

Journal of Energy Storage

journal homepage: www.elsevier.com/locate/est



Research Papers

Equivalent circuit model for electrical performance characterisation of lithium-ion batteries under thermo-mechanical loads

Oscar E. Rojas [a], Ruben Hrstka-Sanchez [a], Feiyang He [a,*], Muhammad A. Khan [a,*]

[a] Centre of Life Cycle Engineering and Management, Faculty of Applied Engineering and Science, Cranfield University, United Kingdom

ARTICLE INFO

Keywords:
Vibration
Thermo-mechanical loads
Equivalent circuit model (ECM)
Electrochemical impedance spectroscopy (EIS)
Hybrid pulse power characterisation (HPPC)
Lithium-ion battery

ABSTRACT

The diverse applications of lithium-ion batteries (LiBs) and the increasing technology for new commercial applications in electric vehicles (EVs) have driven extensive research, expecting to enhance their performance, longevity, and safety. Most of the studies cover the impact of temperature, and only a few encounter the side effects of mechanical vibration. In automotive applications, temperature and vibration have been largely overlooked separately in existing models, leading to unpredictable results. However, when both parameters are reviewed together, they encompass significant variations in resistance, voltage and power. This paper proposes to fill the gap by developing an equivalent circuit model (ECM) that couples temperature and vibration under varying conditions of state of charge (SOC). While many ECMs have been proposed in the literature to improve the battery management system (BMS), none of them have explored the impact of vibrations. The methodology involves the experimental quantification of the cell characteristics by electrochemical impedance spectroscopy (EIS) and hybrid pulse power characterisation (HPPC). The ECM revealed that vibration increased all resistive parameters, particularly at high SOC and low temperature. The quantified variation due to vibration loads is given as the incremental values of the ohmic resistance (R_0), interfacial resistance (R_{int}), diffusion losses (R_1) and capacitance (C_1) (ΔR_0, ΔR_{int}, ΔR_1, ΔC_1), showing an increase with different trends at different temperature and SOC values. At 100% SOC, ΔR_0 varies between 0.67 mΩ at 0 °C to −0.01 mΩ at 40 °C. When the temperature increases, the effects of vibration are less noticeable, proving that temperature is more common in the resistance. Nevertheless, the changes in diffusion resistance and capacitance were complex, with some parameters decreasing under specific conditions. The ECM was validated using three urban dynamometer driving schedule (UDDS) cycles performed at various SOC and temperatures, yielding an average root mean square error of 14 mV, which is of comparable accuracy with other ECMs in the literature.

1. Introduction

The ongoing efforts to reduce CO_2 emissions, driven by standards such as Euro 5 and Euro 6 [1], aim to decrease reliance on fossil fuel imports and mitigate the impacts of global warming [2,3]. This has led to significant growth in the use of EVs, hybrid electric vehicles (HEVs), and plug-in hybrid electric vehicles (PHEVs) over the past decade. Most of these vehicles use LiBs due to their higher energy and power density, higher voltages, and low self-discharge rate [4].

For LiBs to be viable for the application, they must provide and accept power and store energy safely, reliably, and efficiently, which is primarily governed by their internal resistance [5,6]. With batteries ageing through storage and cycling, their performance degrades due to the resistance change. Therefore, it is significant to investigate the resistance behaviour as a decisive characteristic of a lithium-ion cell. Academia and industry have proposed various methods, such as HPPC [7] and EIS [6,8,9], to measure the internal resistance and impedance as direct current (DC) and alternating current (AC) characterisation, respectively.

In addition to storage and cycling, battery resistance is also affected by other parameters such as temperature, SOC, current, and vibrations. The temperature influence is related to chemical reactions occurring in the cells and the ionic conductivities of electrodes and electrolytes [10]. Yue et al. [11] tested three types of lithium batteries: lithium titanium oxide (LTO), lithium iron phosphate (LFP) and lithium nickel cobalt aluminium oxide (NCR) in different ambient temperatures by using a DC internal resistance measurement. They showed that the ohmic internal resistance of the battery grows with the decrease in temperature. They

* Corresponding authors.
E-mail addresses: feiyang.he@cranfield.ac.uk (F. He), muhammad.a.khan@cranfield.ac.uk (M.A. Khan).

https://doi.org/10.1016/j.est.2026.121636
Received 31 January 2025; Received in revised form 25 February 2026; Accepted 15 March 2026
Available online 23 March 2026
2352-152X/© 2026 The Authors. Published by Elsevier Ltd. This is an open access article under the CC BY license (http://creativecommons.org/licenses/by/4.0/).

also noticed that at −30 °C, just below the lowest recommended operating temperature for LIBs, the ohmic internal resistance of NCR LiBs increased dramatically due to the increase of electrolyte viscosity and the decrease of ionic conductivity. Ahmed et al. [12] investigated internal resistances of Lithium Manganese Nickel Oxide (LiMnNiO) and Lithium Iron Phosphate ($LiFePO_4$) batteries at wide temperature ranges from −20 °C to 50 °C. Results highlighted an increase in ohmic resistance and interfacial resistance with a decrease in temperature. High temperatures also appear to impact the resistance of the Lithium-ion battery (LiB). Working at a high temperature leads to an acceleration of the ageing process of the cells, consequently degrading the internal resistance. Leng et al. [13] studied the effect of temperature on the ageing rate of LiBs operating above room temperature using an electrochemistry-based model. The increase of the ohmic, interfacial and diffusion resistance due to cyclic ageing is higher with higher temperatures.

SOC is another parameter affecting the internal resistance of LiBs. However, the ohmic and interfacial resistance present different trends. [5,6] show that the SOC does not impact the ohmic resistance. On the other hand, Seki et al. [14] studied the AC impedance of high-power lithium-ion secondary batteries for the next generation of EVs by measuring the internal resistance. While the ohmic resistance remained constant with the SOC, the interfacial resistance (Rint) tended to decrease with increasing SOC. Kumar et al. [15] also found Rint decreased with SOC, while their results highlighted a slight decrease in the ohmic resistance. Meanwhile, some studies proposed that the interfacial resistance is current-dependent. Its relationship with the current can be described using the simplified Butler-Volmer equation [16,17]. This dependency is negligible at ambient temperature but becomes significant at lower temperatures [6].

The road conditions and the vehicle acceleration generate vibrations that may degrade the lithium-ion battery (LiB) resistance as well [18]. Berg et al. [19] investigated the impact of random vibrations in automotive applications on 18 different lithium-ion 18,650 cell types from seven different manufacturers. Similarly, Lee et al. [20] worked on the vibration-based degradation effect in rechargeable lithium-ion batteries having different cathode materials for railway vehicle applications. The results showed that the resistance increased after two hours of vibrations, especially for batteries with LFP active materials. Hooper et al. [21] tested lithium-ion 18,650 NCA cylindrical cells to multi-axis vibrations and observed an increase in pulse power resistance because of the delamination or cracking of the electrode's surfaces. Another research by Somerville et al. [22] proposed a different degradation mechanism. It revealed that vibration causes the removal of the selectively formed surface film created during a cell's first cycles. The initial film was replaced with the surface film from electrolyte decomposition, which is composed mainly of organic electrolyte decomposition products. Therefore, the cell impedance increased.

The change of the resistance behaviour affects the battery performance, which can be analysed using the different LiB models such as electrochemical, analytical, stochastic, and electrical models [15,16]. ECM, which simulates the battery behaviour, is widely used in the Battery Management System (BMS), the central control unit of the battery pack [13,23]. They can predict the working voltage and power capability depending on the working conditions such as temperature, state of charge (SOC), state of health (SOH) and current [16,24].

Academia has made lots of efforts to develop multiple equivalent circuit models (ECMs) as accurately as possible. Plett [25] developed an approach to estimate the SOC of a LiB through a simple ECM (one RC network) and an Extended Kalman filter (EKF). Gandolfo et al. [26] used two parallel RC networks for their model that tackled mainly the impact of SOC. Similarly, Koseoglou et al. [16] proposed an ECM with two RC networks and an additional resistor compared to the traditional model. Several studies also considered the temperature effect on the model. Tran et al. [24] proposed an ECM with one RC network incorporating the effects of SOH, SOC and temperature on the empirical model parameters. Likewise, Bairwa et al. [27] simulated the performance of NR18650 − 20R LiB at three different temperatures with three parallel RC networks. The precision of the model is said to be improved by increasing the number of parallel RC networks. However, the complexity and processing time also become higher. Another study proposed a coupled equivalent circuit model and convective thermal model to determine the state-of-charge (SOC) and temperature of the LiFePO4 battery working in a real environment with one RC network [28]. These ECMs have been proposed under thermal and current loads at different SOC.

Nevertheless, no ECM was found, including the impact of mechanical vibrations, which have been revealed to have an impact on the LiB performance. Although several studies have reported that mechanical vibrations can alter the internal resistance and interfacial characteristics of lithium-ion batteries, such effects have seldom been incorporated into equivalent circuit models (ECMs) used in battery management systems (BMS). This omission can be attributed to three primary factors. First, the influence of vibration was traditionally regarded as negligible compared to thermal or electrical loads, particularly in the absence of long-term operational data. Second, the simultaneous application and control of mechanical and electrochemical stimuli present experimental challenges, and most standard testing protocols are not configured to impose dynamic mechanical loads. Third, although prior work has demonstrated qualitative changes in impedance under vibration, these effects were not quantified as functions of temperature and state of charge, nor integrated into a parametric framework suitable for real-time modelling.

As battery systems are increasingly deployed in vibration-prone applications like electric vehicles, it is now essential to reconsider this modelling assumption. A mechanistically informed and experimentally supported integration of vibration into ECM parameterisation can enhance the accuracy and resilience of BMS under realistic operating conditions. Therefore, to address the gap, the presented paper aims to develop an ECM with the consideration of the impact of external vibrations induced by the engine and the road conditions [29,30], coupled with temperature under different conditions of SOC.

2. Experimental approach

2.1. Battery specifications

A cylindrical battery was used for the tests. The lithium-ion rechargeable cell is manufactured by Samsung, model INR 18650-20R. The first three letters of the model stand for Lithium (Li), Nickel (Ni) and Round Cell (R). The following four numbers specify an approximate value of the diameter (18 mm) and the length of the cell (65 mm). The last two numbers and the letter R refer to the battery capacity (2.0 Ah). The cell chemistry is denominated as Lithium Nickel Manganese Cobalt Oxide (NMC), referring to the cathode material. The blending chemical composition of Nickel and Manganese influences the performance attributes such as balance capacity, discharge rate and stability. The electrical specifications are listed in Table 1. All cells used in this study were brand new and drawn from the same manufacturing batch. The initial State of Health (SOH) was 100%, and pre-test checks confirmed consistency with the manufacturer's rated capacity and internal resistance.

2.2. Design of experiments

Vibration loads and temperature are two key variables considered in the test affecting the battery's electrochemical properties. Therefore, the Battery cells under different SOC and temperature combinations were characterised. The test SOC ranges from 0% to 100% with a 10% interval. Temperature ranges from −20 °C to 60 °C with a 20 °C step. It covers the typical temperature of EVs under a practical running environment. There are 55 combinations, as shown in Table 2. An

Table 1
Battery specifications [31].

Item specification	Specification
Capacity	2000mAh
Charge	1 A, 4.20 V, Constant-Current-Constant-Voltage (CCCV) 100 mA cut-off,
Discharge	0.2C, 2.5 V discharge cut-off
Nominal voltage	3.6 V
Standard charge	CCCV, 1 A, 4.20 ± 0.05 V, 100 mA cut-off
Rapid charge	CCCV, 4 A, 4.20 ± 0.05 V, 100 mA cut-off
Charging time, Standard charge	180 min / 100 mA cut-off
Charging time, rapid charge	50 min (at 25 °C) / 100 mA cut-off
Max. continuous discharge (continuous)	22 A (at 25 °C), 60% at 250 cycles
Discharge cut-off voltage (end of discharge)	2.5 V
Cell weight	45.0 g max
Height	64.85 ± 0.15 mm
Diameter	18.33 ± 0.07 mm
Charge operating temperature (surface)	Charge: 0 to 50°C
Recommended recharge release (surface)	Recharge <45 °C
Discharge operating temperature (surface)	Discharge: −20 to 75 °C
Recommended re-discharge release (surface)	*Re*-discharge <60 °C

Table 2
Experimental test cell combination.

Temperature (°C)	Battery
-20	S0T-20, S1T-20, S2T-20, S3T-20, S4T-20, S5T-20, S6T-20, S7T-20, S8T-20, S9T-20, S10T-20
0	S0T0, S1T0, S2T0, S3T0, S4T0, S5T0, S6T0, S7T0, S8T0, S9T0, S10T0
20	S0T20, S1T20, S2T20, S3T20, S4T20, S5T20, S6T20, S7T20, S8T20, S9T20, S10T20
40	S0T40, S1T40, S2T40, S3T40, S4T40, S5T40, S6T40, S7T40, S8T40, S9T40, S10T40
60	S0T60, S1T60, S2T60, S3T60, S4T60, S5T60, S6T60, S7T60, S8T60, S9T60, S10T60

independent brand-new cell was assigned to each temperature and SOC combination, resulting in a total of 55 cells tested. The denomination for each cell is the following: the first letter and first number indicate the SOC and the second letter and last figure represent the temperature the battery is exposed to. For example, S2T60 means the tested temperature is 60 °C at 20% SOC.

To quantify the impact of the mechanical loads on the resistance values, the characterisation tests were run before and after the exposure to vibrations. These vibrations due to driving conditions are nondeterministic and, therefore, random in nature. For this reason, the selected load is a random vibration profile rather than a sinusoidal vibration. Therefore, the vibration profile is followed as per standard ISO 12405-1, which is representative of EVs considering induced vibrations from the road and powertrain in the car [32]. The corresponding PSD profile is described in Table 3. The total duration of vibration exposure was 21 h for each test condition.

Table 3
Values for the PSD in the vertical direction [33].

Frequency Hz	PSD g^2/Hz	PSD $(m/s^2)^2$/Hz
5	0.05	4.81
10	0.06	5.77
15	0.06	5.77
200	0.0008	0.08
RMS	1.44 g	14.13 m/s^2

Before the characterisation tests, the slow charge and discharge tests were carried out to calibrate the cells at the desired SOC using the voltage or the Coulomb counting method. The SOC ranges from 0 to 100%, with a step of 10%.

Once the cells were calibrated to the desired SOC value, HPPC and EIS tests were executed to obtain the three resistances R_0, R_{int} and R_1. EIS and HPPC are often described in the literature as two complementary testing methods: while the EIS is accurate for high and mid-frequency losses, the HPPC is more accurate for low-frequency losses [16].

2.3. Slow charge and discharge procedure

The slow charge and discharge test enables parameterising the OCV curve against the SOC values. The OCV is not significantly dependent on temperature [34] and vibration [21]. Therefore, the test is solely run at ambient temperature (20 °C). The test is conducted three times for charge and discharge for consistency and accuracy of results.

The average voltage values for each charge/discharge period are utilised to build the OCV-SOC curve. In this experiment, the charging and discharging rate of C/10 with an ambient temperature of 20 °C is used to obtain the data.

2.4. EIS test procedure

Five EIS tests are running to obtain the resistance values at different SOC levels. Each test is run at a constant temperature.

The procedure of taking the EIS is repeated eleven times from 100% to 0% at increments of 10%. As a result, the cell is charged until 100% and discharged to 90%, 80%, 70%, 60%, 50%, 40%, 30%, 20%, 10% and 0% SOC. Any time the SOC is discharged to 10%, the EIS is measured. A new cell is employed for each temperature to prevent thermal degradation to influence the results. For this reason, the temperature values considered for each test vary in increments of 20 °C, from −20 to 60 °C (−20 °C, 0 °C, 20 °C, 40 °C and 60 °C).

The test procedure is described as follows: Once the cells are calibrated to the desired SOC value, the EIS test is executed. The EIS test enables us to obtain the Ohmic resistance (R_0) and the Interfacial resistance (R_{int}). The EIS test is running five times. Each time at a given temperature.

1. The new cell is charged until 100% SOC with a rate current of 1C (2 A) at a constant voltage of 4.2 V. The discharging stops once the current drops below 200 mA.
2. A relaxation period of one hour is given for one cell.
3. The EIS measurements are taken in a frequency range from 5 kHz to 2mHz at 100% SOC.
4. The battery is discharged to the next SOC level (90%) at a 1C current rate. The discharging stops once the current drops below 200 mA.
5. The EIS measurements are taken for 90% SOC in a frequency range of 2mHz to 5 kHz.
6. A relaxation period of one hour is given for the cell before discharging it again.

The EIS test procedure is run again after the vibration test is conducted. Measuring the EIS after exposure to vibrations enables the quantification of their impact on R_0 and R_{int}. The EIS post-vibrations are run at 0 °C, 20 °C and 40 °C (a range of temperatures a battery is frequently exposed to) from 100% to 0% SOC. It focused the statistical comparison on the operative temperature window while minimising extreme-temperature confounders.

2.5. HPPC test procedure

The HPPC is a current pulse method utilised to calculate the dynamic properties of the battery. It enables the determination of the diffusion

parameters of the ECM R_1 and C_1. In this test, a series of 30-s discharge pulses of 5 A are applied for each SOC value. Initially, the battery is calibrated to 100% SOC. After an hour of relaxation period to reach the battery equilibrium, the first pulse is obtained. Then, a resting time of 1 h is given to the battery. After that, the battery is discharged at a 0.5C rate to achieve 90% SOC. This procedure is repeated in intervals of 10%, eleven times, from 100% SOC to 0% SOC.

The HPPC is run again after the vibration test to measure the difference in resistances and capacitances ΔR_1 and ΔC_1 to quantify the impact of vibrations on the diffusion behaviour of the cell.

Once the experiment is conducted, the data is exported to MATLAB to use the curve fitting options (*nlinfit*) to determine the parameters R_1 and C_1. They are identified by fitting the voltage response of the cell during the relaxation period of the HPPC test (cf. HPPC test) with the overpotential corresponding to the diffusion behaviour in the ECM. The "nlinfit" function in MATLAB is based on the Levenberg-Marquardt algorithm, a popular method combining the concepts of gradient descent and the Gauss-Newton method.

2.6. Experimental setup

To run the different tests, a potentiostat 5000 from Gamry Instruments with a resolution of 12.5 μV/bit and a measurement accuracy of ±1 mV in Fig. 1(a) is used to apply a desired voltage and current to the cell and study its response. The maximum voltage limit is 6 V, and the maximum current is 5 A. For an EIS characterisation, the frequency ranges are given from 5 kHz to 2mHz.

The potentiostat is connected from one end to the Gamry Universal Battery Holder holding the cell being tested. The cell and the battery holder are placed in a thermal chamber where the temperature can be controlled. The other end of the potentiostat is connected to a computer with software for data acquisition, as depicted in Fig. 1.

2.6.1. Pre-vibration experimental setup

For the experiments, an ECO MT135 ambient chamber was utilised to control temperature in a wide range between 60 °C and − 20 °C, as shown in Fig. 1(a). It delivers uniform and constant temperature during the experiment and also acts as a Faraday cage to avoid electromagnetic noise.

Inside the ambient chamber, the battery holders connect a cell, as presented in Fig. 1(b). Depending on the program setup, current and voltage are induced by the potentiostat. Then, the current and voltage response is captured by the Gamry software. All measurements in this setup were performed on brand new cells from the same batch as specified in Section 2.1.

2.6.2. Vibration experimental setup

For the post-vibration test, a shaker and a battery controller are added for the vibration setup, as illustrated in Fig. 2(a). A prototype battery with two modules inside, each module with six cells, for a total of 12 cells. The battery pack prototype is allocated inside the ambient chamber with an accelerometer, as is presented in Fig. 2(b).

The shaker controller with the adapted software allows the input of the random vibration profile for the experiment. The power spectral density (PSD) is selected from the standard ISO 12405 in the vertical direction. The experiment is conducted in cells at different temperatures and levels of SOC. The overall schematic for the pre-vibration and post-vibration experiments is illustrated in Fig. 3.

2.7. ECM development for pre- and post-experiments

2.7.1. Proposed ECM

The ECM chosen is represented in Fig. 4. It is composed of a voltage source, an ohmic resistance R_0, an interfacial resistance R_{int} and one RC branch to model the diffusion behaviour of the cell. [16,26] worked with a similar model as it presents an interesting balance between precision and simplicity. The mid-frequency losses associated with the charge transfer are sometimes represented by a double-layer capacitance. However, since the time constant of the double-layer capacitance is low, it can be omitted [6,16].

The ECM is governed by Kirchhoff's voltage law (Eq. 1):

$$V_{out} = V_{OCV} - (R_0 I + R_{int} I + V_1) \tag{1}$$

V_{out}: Output voltage of the cell
V_{OCV}: Open-circuit voltage
I: Imposed current
R_0: Ohmic resistance
R_{int} : Interfacial resistance
$\boldsymbol{V_1}$: Overpotential due to R_1C_1 (1).
One overpotential can be written as Eq. 2:

$$V_i = IR_i\left(1 - \exp\left(-\frac{t}{R_i C_i}\right)\right) \tag{2}$$

V_i: Voltage of the RC branch
I: Imposed Current
R_i: Resistance of the RC branch
C_i: Capacitance of the RC branch
$\boldsymbol{t}$: time (2).
Therefore, the governing equation of the ECM is shown in Eq. 3:

$$\boldsymbol{V_{out} = V_{OCV} - I\left(R_0 + R_{int} + R_1\left(1 - \exp\left(-\frac{t}{R_1 C_1}\right)\right)\right)} \tag{3}$$

The parameters of the governing equation are determined

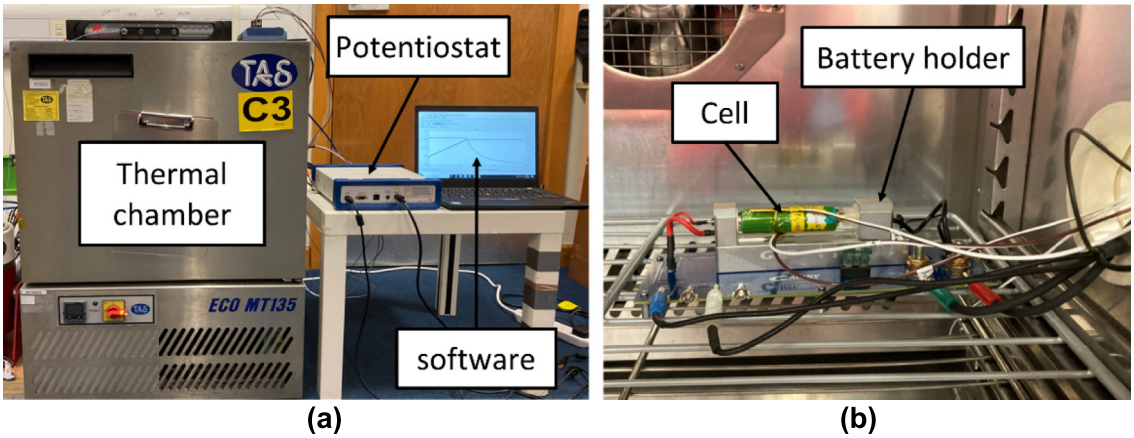


Fig. 1. (a) Thermal chamber, potentiostat and software. (b) Battery holder and cell inside the thermal chamber.

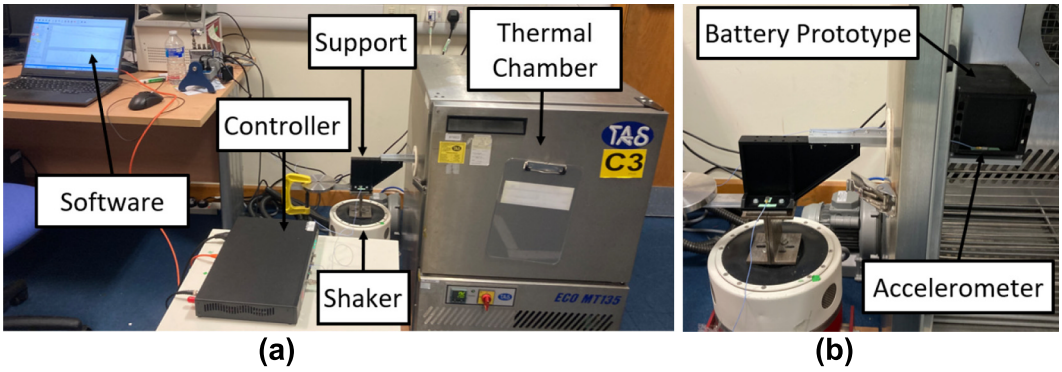


Fig. 2. (a) Overall vibration testing setup. (b) battery prototype and accelerometer inside the chamber.

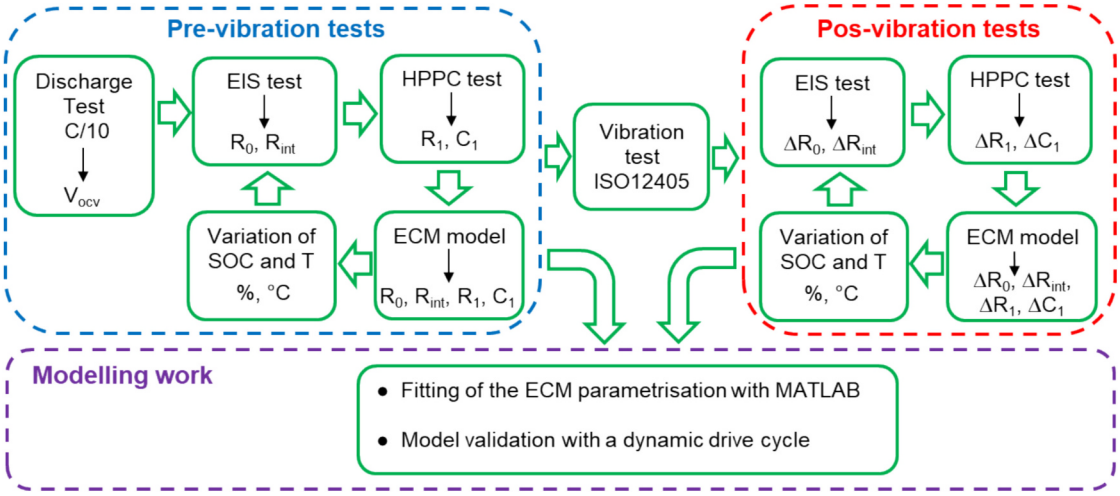


Fig. 3. Schematic of experiments.

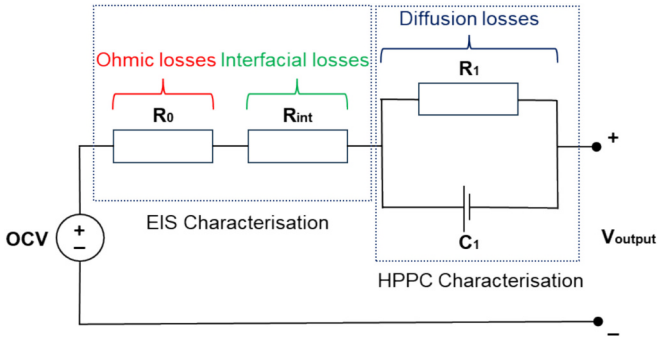


Fig. 4. Schematic of the ECM.

experimentally, as detailed in Sections 2.7.2 and 3.5.

2.7.2. Parameter identification of the ECM equation

Three different experiments are conducted to calculate the parameters of the ECM governing equation:

1. Open-Circuit Voltage (OCV): Determined by running a slow charge and discharge test to measure the OCV as a function of the State of Charge (SOC). Temperature and vibrations do not significantly impact the OCV. Therefore, the OCV–SOC relation was obtained before vibration exposure and treated as vibration-insensitive in this work in line with prior evidence [21].
2. Ohmic Resistance R_0 and Interfacial Resistance Rint: Determined by Electrochemical Impedance Spectroscopy (EIS) at different SOCs and temperatures before and after exposure to vibrations.
3. Resistance-Capacitance pair R_1C_1: Determined by running a Hybrid Pulse Power Characterisation (HPPC) test, which is more precise than EIS for capturing the cell's diffusion and dynamic behaviour [35,36].

A second-order polynomial eq. 4 is chosen to represent the relationship between the resistances/capacitances and the temperature, SOC and vibrations. It enables optimisation of the two requirements for the BMS: to present a low computational complexity for swift calculations of the battery constants and, at the same time, a high precision (first-order equations appear to already be quite accurate, as per [24]). The parameter equation for the ECM is:

$$P = p_0 + p_1 T + p_2 SOC + p_3 T^* SOC + p_4 T^2 SOC + p_5 SOC^2 T + p_6 T^2 + p_7 SOC^2 + p_8 SOC^2 T^2 + \Delta P_{vib} \quad (4)$$

P: Parameter of the ECM (resistance or capacitance)
T : Temperature
SOC : State-of-Charge
$T^i * SOC^j$: The interaction term between temperature and SOC.
ΔP_{vib}: Variation of the considered parameter due to vibrations.
$p_0, p_1, p_2, p_3, p_4, p_5, p_6, p_7, p_8$: Constants (determined by fitting the equation to the experimental curves).

3. Results and discussions

3.1. Slow charge and discharge test

The OCV curve obtained in Fig. 5 presents an incremental exponential curve where a ramp variation is given at a low state of charge (i.e., 0% - 6%). After that, the curve continues with an increasing trajectory in a linear trend until the cell reaches its full charge. This pre-vibration OCV–SOC characterisation provides the calibration basis for subsequent modelling. The profile can be compared with another research [37,38] to confirm its trajectory.

Finally, after multiple charge and discharge tests in different cell samples, the maximum experimental capacity of the cell reaches 2.08 Ah, which is slightly superior to the nominal value of 2 Ah. The discharge rate gives this small variation between the experimental and nominal capacity. Liu et al. [39] obtained the discharge characteristics of a lithium titanate oxide battery at different discharge rates, proving that the discharge capacity decreases when the charge rate increases.

3.2. EIS test (influence of temperature and SOC on the resistances R_0 and R_{int})

The impedance spectrum of the battery is obtained by performing the measurement described in Section 2. The results of the EIS are given for 11 states of charge in increments of 10% from 0% to 100% at temperatures between −20 °C to 60 °C. The Nyquist plots (Fig. 6) exhibit consistent features across all conditions, including an ohmic resistance (R_o) at the high-frequency intercept, a semicircle representing charge transfer resistance (R_{int}), and a low-frequency tail associated with diffusion.

At low temperatures (−20 °C and 0 °C), the ohmic resistance R_o remains nearly constant with respect to SOC (e.g., ≈18 mΩ at −20 °C), while the semicircle radius increases markedly at lower SOC, indicating a rise in R_{int}. These trends are consistent with literature findings [40–43]. As the temperature rises, R_o slightly decreases (to ≈12 mΩ at 20 °C), and the semicircle becomes less pronounced, indicating improved interfacial kinetics and reduced R_{int}.

Notably, the local minimum in Im(z), corresponding to the direct current resistance (DCR), shifts towards lower Re(z) with increasing temperature and becomes less distinguishable above 40 °C. This behaviour confirms that interfacial resistance is strongly temperature dependent, whereas R_o remains largely unaffected by thermal conditions. The SOC dependence persists at all temperatures, with impedance values increasing monotonically at lower SOC. These baseline results serve as reference conditions for isolating and quantifying the effect of mechanical vibration in subsequent sections.

The plots of R_0 and R_{int} against SOC for different values are visible in Fig. 7 and Fig. 8, respectively. The values of R_0 and R_{int} have been calculated by a MATLAB code.

R_0 appears to be constant at a given temperature for all the SOC values. Hence, SOC does not seem to impact the ohmic resistance.

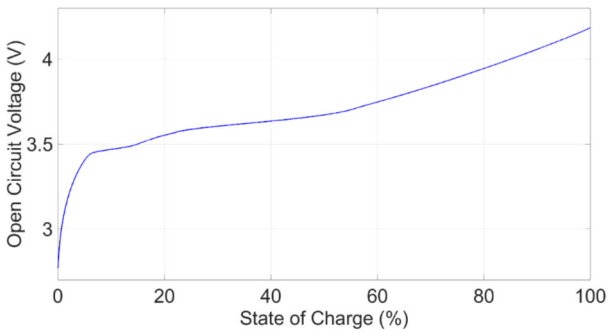


Fig. 5. OCV-SOC curve.

Temperature does not affect R_0 much, with a slight increase in resistance as the temperature drops. R_0 value reaches nearly 20 mΩ at −20 °C, only a few mΩ (7mΩ to 5mΩ) compared to the other temperatures. Nevertheless, R_{int} is more temperature-dependent than R_0. Fig. 8 clearly highlights the increase in interfacial resistance as the temperature lowers. For low SOC levels, R_{int} reaches 140 mΩ. While R_{int} is steady for high and medium, SOC values always increase at lower SOC levels. The phenomenon is emphasised, especially at lower temperatures. At −20 °C, R_{int} presents a little decrease at 70% and 60% SOC before rising again. This could be attributed to the complexity of keeping the temperature constant at −20 °C during the EIS experiment.

R_0 includes the resistance of the electrolyte, current collectors and terminals. However, during the battery operation, the change in R_0 is triggered mainly by the electrolyte [44]. By decreasing the temperature in the cell, the density and viscosity of the electrolyte are augmented, causing an increase in the concentration of lithium-ion (Li^+), facilitating the conductivity and reducing the resistance. Considering that the terminals are made of metals where the electrical conductivity depends on the temperature, it can be assumed that the terminals are contributors to the changing resistance R_0. Hence, when the temperature of the terminals increases, their electrical conductivity decreases, reducing the magnitude of R_0.

The semicircle in the Nyquist plot represents the double-layer capacity and charge transfer process at the electrode-electrolyte interface. Since both the anode and the cathode contribute to the semicircle, both include the surface film resistances and internal charge transfer resistances [45]. An increase in R_{int} is observed during the increase in temperature, and it is easy to identify as the semicircle enlarges. This electrochemical process is temperature-dependent because the transfer of electrons and lithium ions depends on the conductive agent and the bond of the active material. In this case, the active material lattice shrinks due to the lower temperature, hindering the inter-transfer of lithium-ions in the cathode or, inversely, the transfer-inter in the anode.

Fig. 9 and Fig. 10 account for the temperature and the SOC to provide values of R_0 and R_{int}. It can be observed that the lower the temperature, the higher the resistances R_0 and R_{int}. Conversely, the higher the SOC, the lower the resistances R_0 and R_{int}. It is noticeable that the temperature is much more influential than the SOC in the resistance change. This phenomenon is due to the increase in viscosity of the electrolyte of the battery. The density of the conductive material hinders the flow of the ions.

3.3. HPPC test (influence of the temperature and SOC in R1 and C1)

An example of a 30-s pulse and the relaxation period of one hour from the HPPC is shown in Fig. 11. The massive drop in the voltage is due to the 5 A direct current pulse applied to the cell. The values of R_1 and C_1 are represented in Fig. 12 and Fig. 13.

Potrykus et al. [46] developed a model incorporating diffusion resistance to obtain better results in different domains and industry applications. The HPPC experiments proved that the SOC is negligible in calculating R_1. In the same way, the results depicted in Fig. 12 are sound with respect to other authors. However, it is not the same as the temperature that directly influences ionic diffusion.

The first noticeable trend is the opposite variation between R_1 and C_1: as R_1 rises, C_1 reduces inversely. R_1 is more consistent at lower temperatures, while it lowers as the SOC decreases. The highest value of resistance is reached at 100% SOC and temperature 0 °C (i.e., 884 mΩ). C_1 increases with low values of SOC, especially 10% and 0%. A little decrease can be observed in C_1 as temperature rises.

Sungur et al. [47] conducted experiments to evaluate the effects of temperatures (−10 °C, 25 and 40 °C) in an INR18650A28 lithium-ion cylindrical cell. Their results show that the temperature impacts the parameters R_1 and C_1 at different values of SOC. For R1, the values increase at lower temperatures, where variations at medium values of SOC (from 20% to 60% SOC) are more noticeable. Meanwhile, C_1 presents an

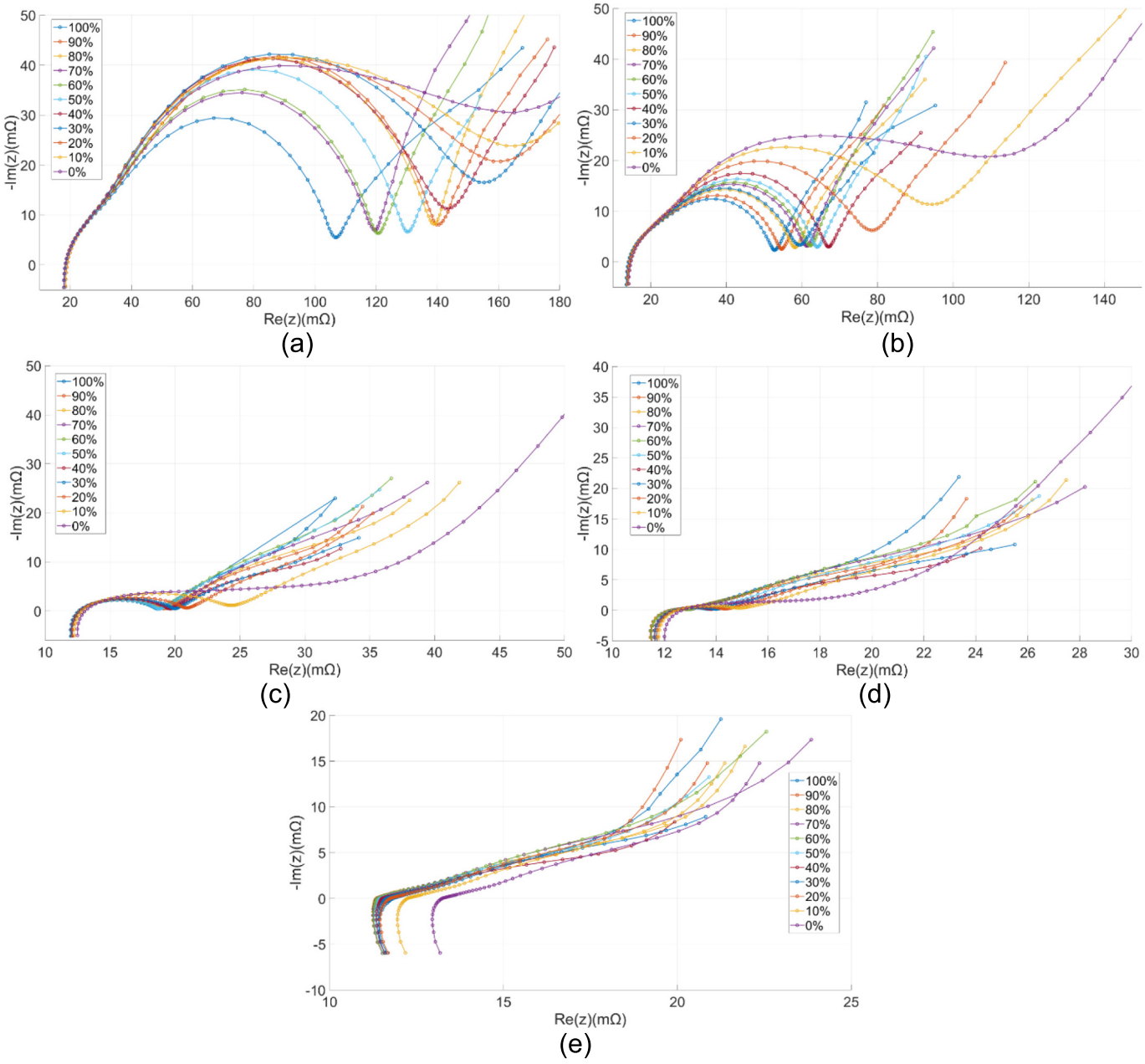


Fig. 6. Nyquist plots against for (a) -20 °C, (b) 0 °C, (c) 20 °C, (d) 40 °C and (e) 60 °C.

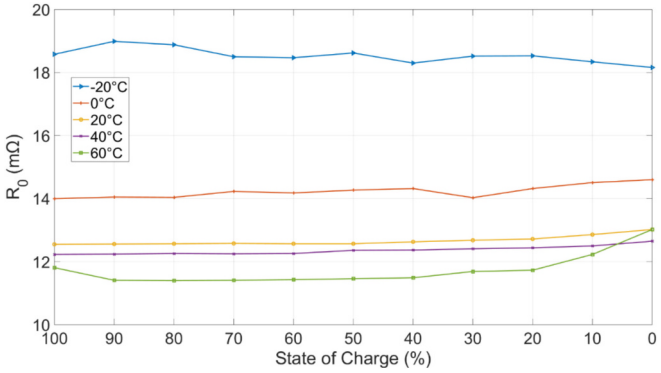


Fig. 7. R_0 plot against SOC values for −20 °C, 0 °C, 20 °C,40 °C and 60 °C.

increment at lower temperatures as well, but the SOC magnitude remains steady. In this study, it is appreciated that similar behaviour for R_1 and C_1, and therefore, the results shown are sound and consistent with previous research.

3.4. *Pre-vibration modelling results*

To determine the constants of the quadratic equation (Eq. 5) for R_0, Rint, R_1 and C_1, the following matrix system is solved, and the results are shown in Table 4:

$$\mathbf{A} = \mathbf{XB} \tag{5}$$

A: Matrix containing the quadratic function variables (T, SOC, SOC^2, T^2, …)

X: Matrix containing the unknown constants p0, p1, …, p8

B: Matrix containing the experimental parameter values.

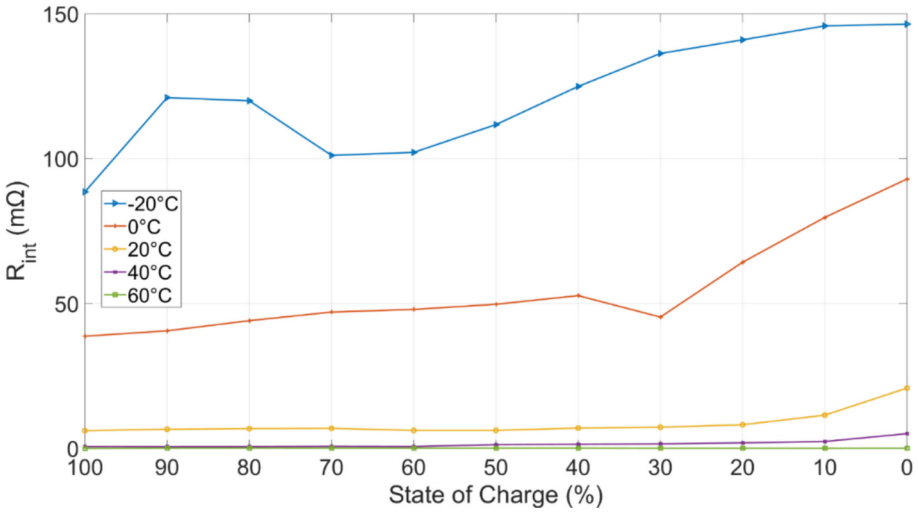


Fig. 8. Rint plot against SOC values for −20 °C, 0 °C, 20 °C,40 °C and 60 °C.

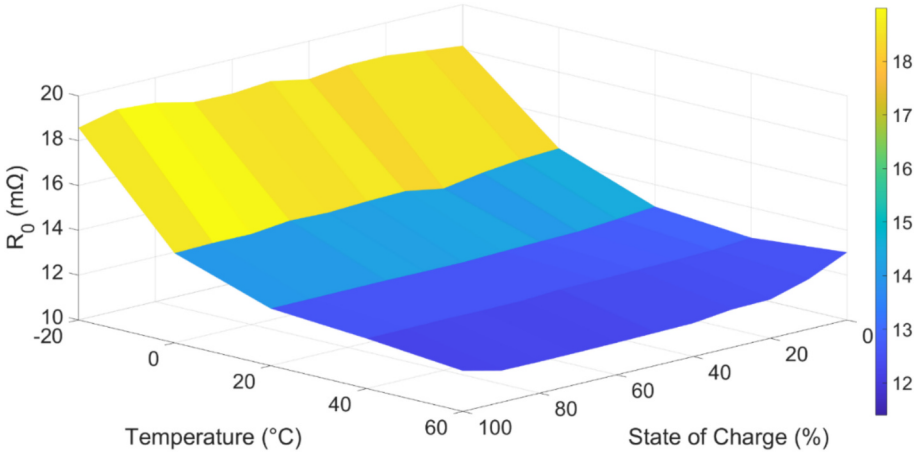


Fig. 9. 3D representation of R_0 versus SOC and temperature.

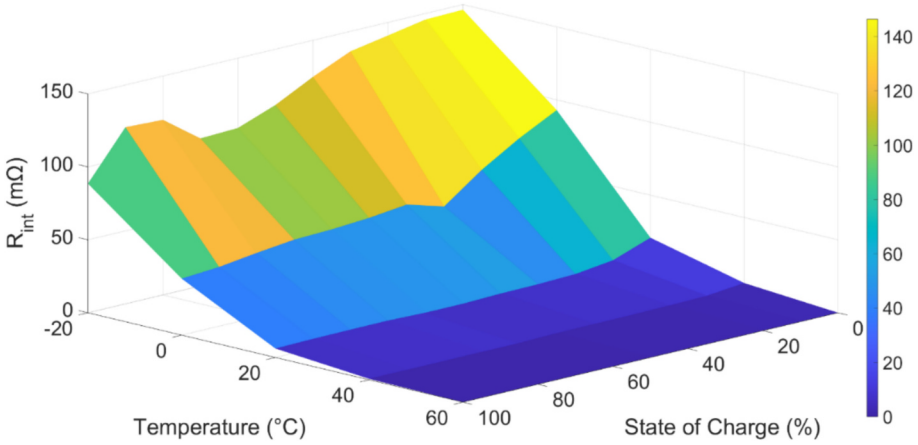


Fig. 10. 3D representation of R_{int} versus SOC and Temperature.

3.5. *Influence of vibration on the battery*

The EIS and HPPC tests have been conducted again after the cells have been exposed to the vibration test at different temperatures (0 °C, 20 °C and 40 °C) and SOC levels (from 100% to 0%C) to focus the statistical comparison on the EV's operative temperature window while minimising extreme-temperature confounders. To quantify the impact of vibrations with temperature and SOC, ΔR_0, ΔR_{int}, ΔR_1 and ΔC_1 (representing ΔP_{vib} in the parameter equation of the ECM) have been computed. They represent the difference between the resistance value

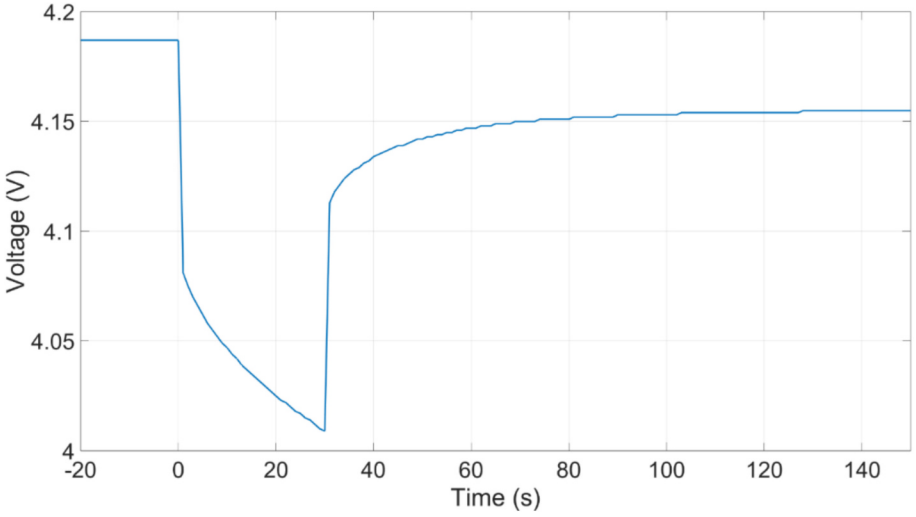


Fig. 11. Voltage response at 20 °C and 100% SOC.

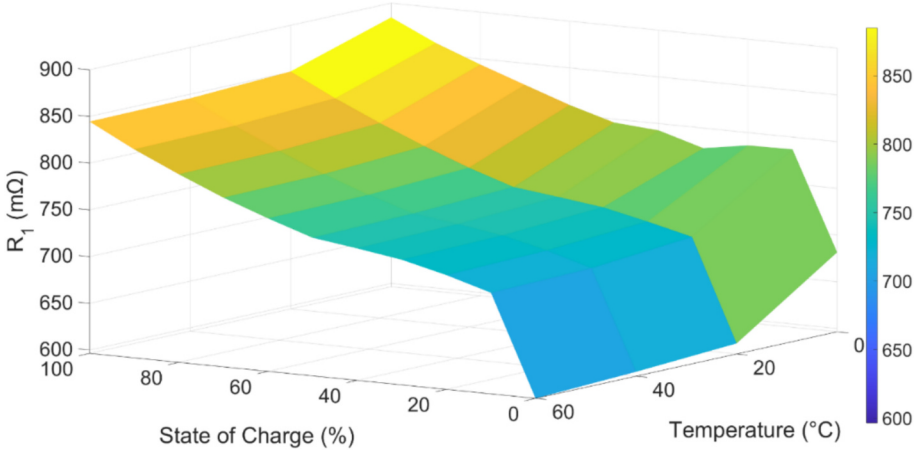


Fig. 12. 3D representation of R_1, SOC and temperature.

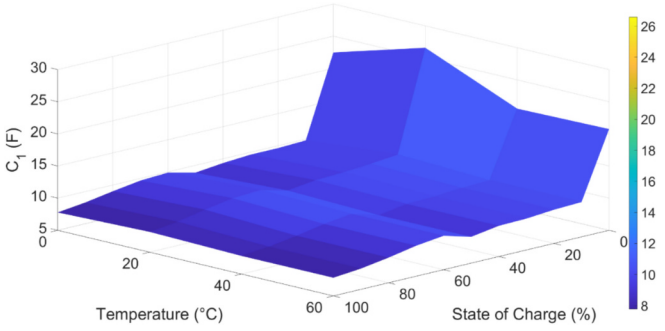


Fig. 13. 3D representation of C_1, SOC and temperature.

post-vibration and the resistance value pre-vibration.

3.5.1. *Variation in the resistances ΔR_0 and ΔR_{int}*

The induced vibration in the cells proved to affect the ohmic and interfacial resistance, and the variation calculations are presented in Fig. 14 for ΔR_0 and in Fig. 15 for ΔR_{int}.

The vibrations showed a greater impact on ΔR_{int} compared to ΔR_0, especially at 0 °C. More specifically, the increase in resistance R_0 and R_{int} is significant at 0 °C from 100% SOC to 70% SOC. The highest value of ΔR_{int} is given at 90% SOC with a value of 13.25 mΩ, and ΔR_0 is given at 100% SOC with a value of 0.67 mΩ.

Table 4
Pre-vibration constant values R0, Rint, R1 and C1 for the quadratic equation.

P	R_0	R_{int}	R_1	C_1
P_0	14.8735	78.2082	723.9729	17.4903
P_1	−0.1281	−3.194	−3.8856	0.0741
P_2	−0.0001	−0.7897	1.8057	−0.2833
P_3	−0.0003	0.0111	0.0428	−0.0013
P_4	0	0.0001	−0.0005	0
P_5	0	0	−0.0002	0
P_6	0.0016	0.0315	0.0429	−0.0017
P_7	0	0.0046	−0.0033	0.0021
P_8	0	0	0	0

ΔR_0 and ΔR_{int} reached lower values from 70% to 0% SOC before and after exposure to vibrations, indicating that vibration is less severe in this range of SOC. Nevertheless, at 30% SOC, ΔR_0 and ΔR_{int} showed a peak, and then the resistance dropped again.

It is appreciated that in all temperature cases, ΔR_0 and ΔR_{int} globally diminish as SOC decreases, reaching even negative values for low SOC, which indicates that the resistance post-vibration is lower than the resistance before exposure to vibration.

These behaviours may be attributed to microstructural changes in

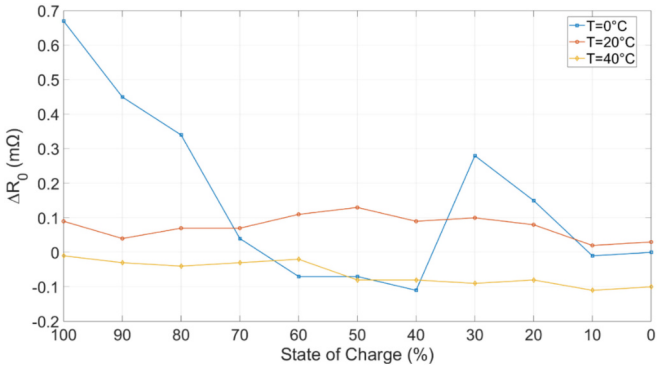


Fig. 14. Resistance's variation ΔR_0 with respect to SOC and temperature.

the electrode materials induced by mechanical stress. As reported by Lee et al. [20], vibration leads to an increase in internal resistance across various lithium-ion chemistries, a trend consistent with the present findings. Structural degradation, including the development of micro-cracks, particle detachment, and fragmentation within the anode and cathode materials, can reduce conductive pathways and increase local resistances [30,48]. Moreover, the dislodged particles may interact with the electrolyte, contributing to the growth of additional SEI (solid electrolyte interface) layers, which increases interfacial resistance. The impact is particularly significant at high SOC levels and low temperatures, where the electrode structure is more mechanically stressed and brittle.

Furthermore, vibration is known to affect not only individual cells but also the integrity of electrical contacts at the module and pack level. As highlighted in [49], long-term vibration exposure can degrade the mechanical stability of welded or bolted connections, further increasing contact resistance. Although our current study focuses on single-cell analysis, such systemic degradation phenomena may partially explain the observed resistance trends.

3.5.2. *Variation in the resistance ΔR1 and capacitance ΔC1*

Fig. 16 and Fig. 17 depict the variations in diffusion resistance (ΔR_1) and capacitance (ΔC_1) across SOC and temperature conditions.

At temperatures of 0 °C, the variation in diffusion resistance ΔR_1 is quite significant from 100% to 60% SOC. From 60% to 10%, ΔR_1 is closer to 0 mΩ, reaching even slight negative values, indicating a lower diffusion resistance after exposure to vibrations. Nevertheless, at 0% SOC, ΔR_1 rises again to nearly reach 100 mΩ. At temperatures of 20 °C and 40 °C, ΔR_1 variations are more moderate and closer to 0 mΩ from 100% to 10%. However, at 0% SOC, ΔR_1 becomes negative for

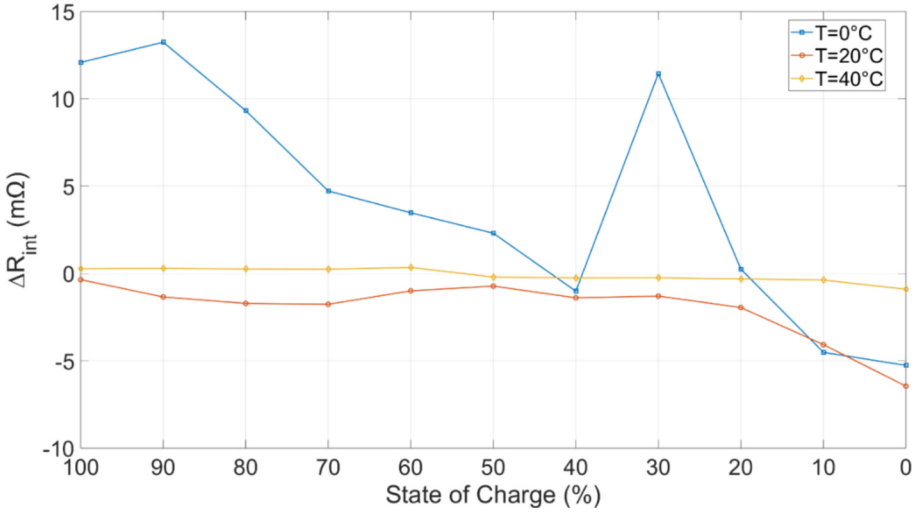


Fig. 15. Resistance's variation ΔR_0 with respect to SOC and temperature.

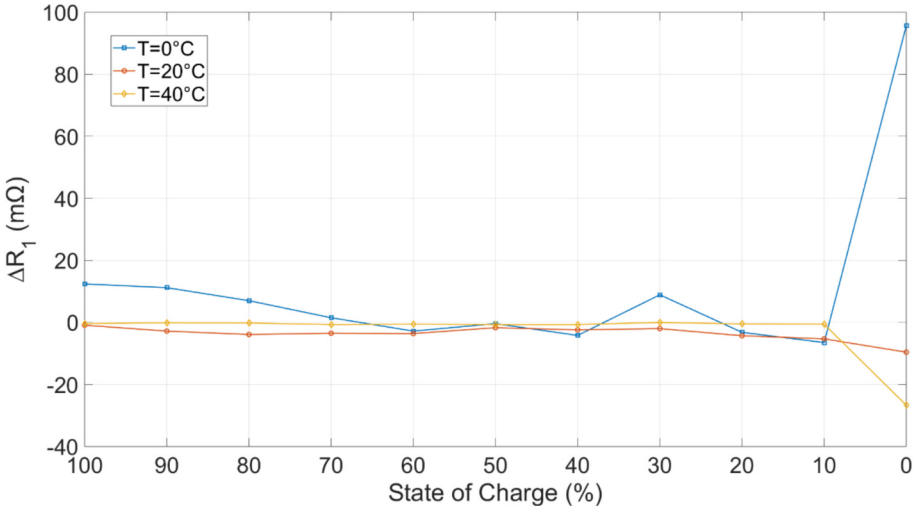


Fig. 16. ΔR_1 plot against SOC for $T = 0$ °C, $T = 20$ °C and $T = 40$ °C.

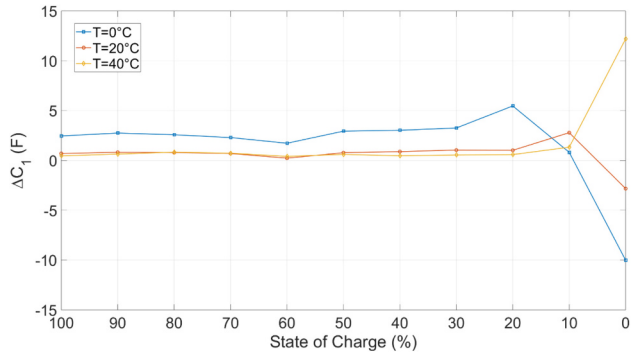


Fig. 17. ΔC_1 plot against SOC for T = 0 °C, T = 20 °C and T = 40 °C.

temperatures of 20 °C and 40 °C with a noticeable drop in the graph. Conversely, a massive jump in the positive scale is depicted for 0 °C.

The variation in the capacitance, ΔC_1, is small but positive for all temperatures from 100% to 10%, indicating that vibration is acting upon the capacitance. The highest values are reached at the temperature of 0 °C (2.46 F), suggesting that the capacitance inside the battery increases at lower temperatures with vibration.

The discontinuities observed in both ΔR_1 and ΔC_1 at 0% SOC suggest unstable electrochemical conditions in a deeply discharged state. At such low SOC, lithium inventory is depleted, and the electrode materials are electrochemically saturated, potentially disrupting ionic diffusion mechanisms and altering double-layer capacitance. Additionally, the mechanical agitation induced by vibration may accentuate these effects by modifying local porosity or electrolyte distribution. Although our experimental setup does not allow direct observation of these internal processes, similar behaviours have been reported in the literature [50], reinforcing the interpretation that mechanical vibrations can perturb the dynamic properties of the cell.

While the present results reflect the electrochemical impact of vibration at the single-cell level, their extension to module or pack assemblies requires caution. Structural damping, mechanical constraints, and multi-point interconnections in higher-level systems can alter the propagation and intensity of vibrational energy [51–54]. These effects may attenuate or redistribute mechanical loads, reducing their local influence on individual cells. Further investigation at the module and pack level is therefore essential to assess the net effect of structural integration on vibration-induced degradation mechanisms.

3.6. Post-vibration modelling results

ΔR_0 and ΔR_{int} can be quantified with a polynomial equation. A first-order equation might not be precise, so a quadratic function is introduced to give the smooth and gradual variations of ΔR_0 and Δ_{Rint}. Fitting ΔR_0 and ΔR_{int} with a quadratic function on MATLAB leads to the following expressions (Eqs. 6 and 7):

$$\Delta R_0 = 0.1303 - 0.0046*T - 0.0098*SOC + 0.0010*T*SOC + 0.0001*SOC^2 \quad (6)$$

$$\Delta R_{int} = -3.7611 - 0.2346*T - 0.1567*SOC + 0.0013T*SOC - 0.0001T*SOC^2 + 0.0077*T^2 - 0.0001*T^2*SOC \quad (7)$$

The coefficients of determination R^2 are 0.78 and 0.77, respectively, for ΔR_0 and Δ_{Rint}.

The results of the fitting procedure are visible in Fig. 18 for ΔR_0 and Fig. 19 for ΔR_{int}.

The variations due to vibrations ΔR_1 and ΔC_1 can be fitted with a quadratic function as follows:

$$\Delta R_1 = 54.6594 - 2.2223*SOC + 0.0192*SOC^2 - 4.4655*T + 0.1679*T*SOC - 0.0014*T*SOC^2 + 0.0677*T^2 - 0.0025*T^2*SOC \quad (8)$$

$$\Delta C_1 = -4.6614 + 0.2924*SOC - 0.0024*SOC^2 + 0.1178*T - 0.0100*T*SOC + 0.0001*T*SOC^2 + 0.0047*T^2 - 0.0001*T^2*SOC \quad (9)$$

Although the ECM and the polynomial parameterisation adopted in

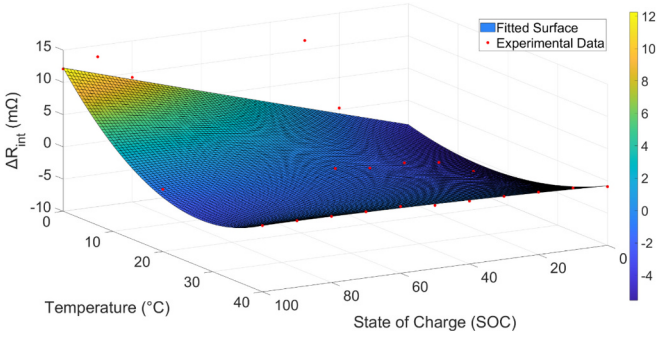


Fig. 19. Fitted surface for ΔR_{int} with experimental points (b).

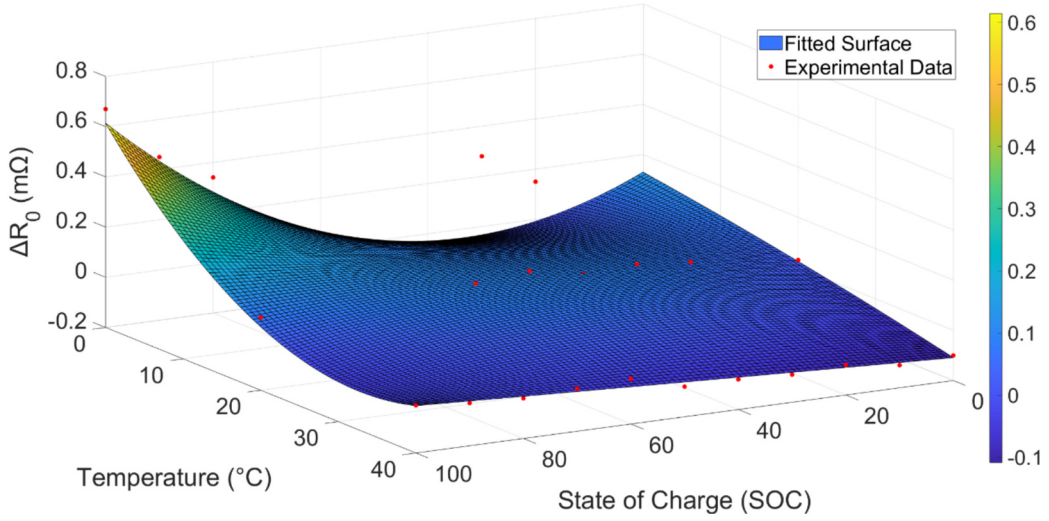


Fig. 18. Fitted surface for ΔR_0 with experimental points.

this study follow a conventional mathematical structure, the novelty of this work lies in the experimental coupling of vibration, temperature, and SOC effects into a unified equivalent circuit framework. This integration enables the quantification of thermo-mechanical influences on the electrical response of lithium-ion cells, which has not been experimentally demonstrated in previous studies. The use of a second-order polynomial ensures a practical trade-off between model accuracy and computational efficiency, allowing direct implementation within real-time BMS algorithms.

3.7. Model validation

To validate the proposed ECM, which was derived by substituting Eq. 4 into Eq. 3, the battery cell has been subjected to an Urban Dynamometer Driving Schedule (UDDS) cycle, which is a dynamic "city test" representing city driving conditions. The input current profile is visible in Fig. 20. Three validation tests were performed at different temperature and initial SOC combinations, values different from those in the experimental scheme conducted. The validation scheme is summarised in Table 5.

The resulting output voltage from the experimental cell and the model is visible in Fig. 21 for correlation.

The model presents a good accuracy that can be quantified by the Root Mean Square Error (RMSE) and the mean absolute percentage error (MAPE) using Eqs. 11 and 12:

$$\boldsymbol{RMSE} = \sqrt{\frac{1}{\boldsymbol{N}} \sum_{i=1}^{\boldsymbol{N}} (\boldsymbol{Vi, experimental} - \boldsymbol{Vi, model})^2} \tag{11}$$

N: Number of values
$V_{i,\ experimental}$: Experimental voltage value
$V_{i,\ model}$: Model voltage value

$$\boldsymbol{MAPE} = \frac{1}{\boldsymbol{N}} \sum_{i=1}^{\boldsymbol{N}} \left| \frac{\boldsymbol{Vi, model} - \boldsymbol{Vi, experimental}}{\boldsymbol{Vi, experimental}} \right| \tag{12}$$

The average RMSE of the three validation scenarios is equal to 14 mV, which is in the range of the proposed models obtained in the literature [55] and the average MAPE is inferior to 0.24 with a unified electric storage system (UESS) model. Model from [24] integrating SOH effects reached an RMSE in the range of 10-15 mV.

To measure the impact of the vibrations on the accuracy of the model, their effect has been suppressed to measure the RMSE, taking into account only temperature and SOC. It appears that the average RMSE reaches 19 mV, which represents an increase of 26%. Thus, including the vibrations is significant.

Table 5
Validation test scheme.

Validation scenario	Temperature (°C)	Initial SOC (%)
1	10	85
2	25	65
3	35	75

The error between the model and the experimental data might come from the fact that close to the voltage cut-off value of 4.2 V (100% SOC), the model overestimates the capacity of the battery to increase its voltage compared to the experimental data. Another explanation for the error encountered may come from the fact that other factors, such as current and SOH, do impact the parameters of the ECM and have not been considered in this research.

In terms of practical deployment, the proposed model can be feasibly integrated into BMS without additional hardware requirements. Modern EVs are already equipped with inertial measurement units (IMUs) or tri-axial accelerometers for control and safety applications. These sensors can supply vibration data in statistical form, such as RMS acceleration or power spectral density, sufficient for the parametrised ECM. The model's formulation ensures low computational complexity, suitable for real-time processing. Given that neglecting vibration increases RMSE by 26%, the inclusion of vibration effects is justified in applications demanding high predictive accuracy and operational robustness.

4. Conclusions

The present work provides a comprehensive analysis of the factors that influence the electrical performance of lithium-ion batteries, particularly focusing on the combined impacts of temperature, SOC, and mechanical vibrations. With the experimental tests, the paper proposed an ECM model considering the vibration influence.

Through EIS and HPPC experiments, it was found that temperature significantly affects the battery's internal resistances and capacitance, with lower temperatures leading to higher resistances due to reduced ionic mobility and slower charge transfer processes. The SOC also plays a crucial role in the cell resistance. It was observed that the R_{int} increases at lower SOC levels, likely due to changes in the SEI and electrode materials' behaviour.

After applying mechanical vibrations, it was observed that further complications of the performance characteristics of the battery led to

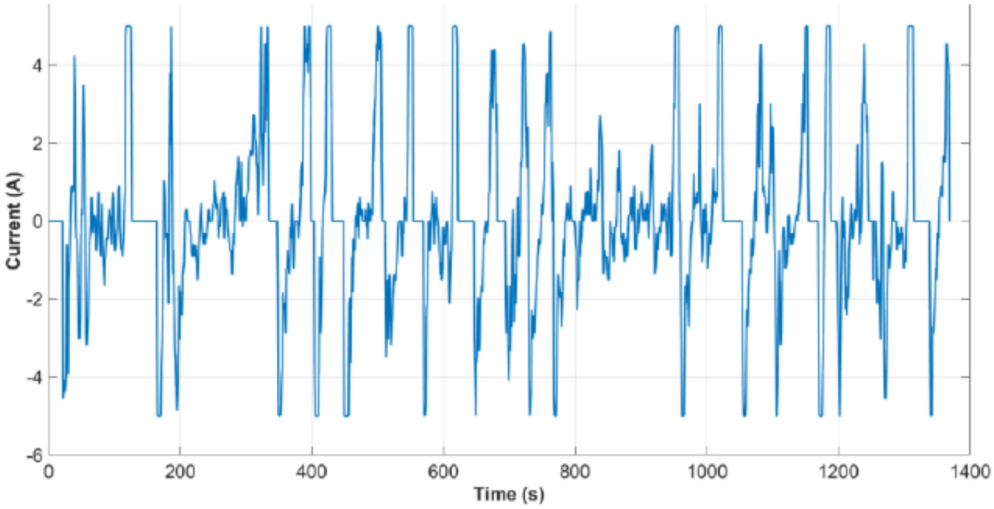


Fig. 20. Dynamic current profile for model validation.

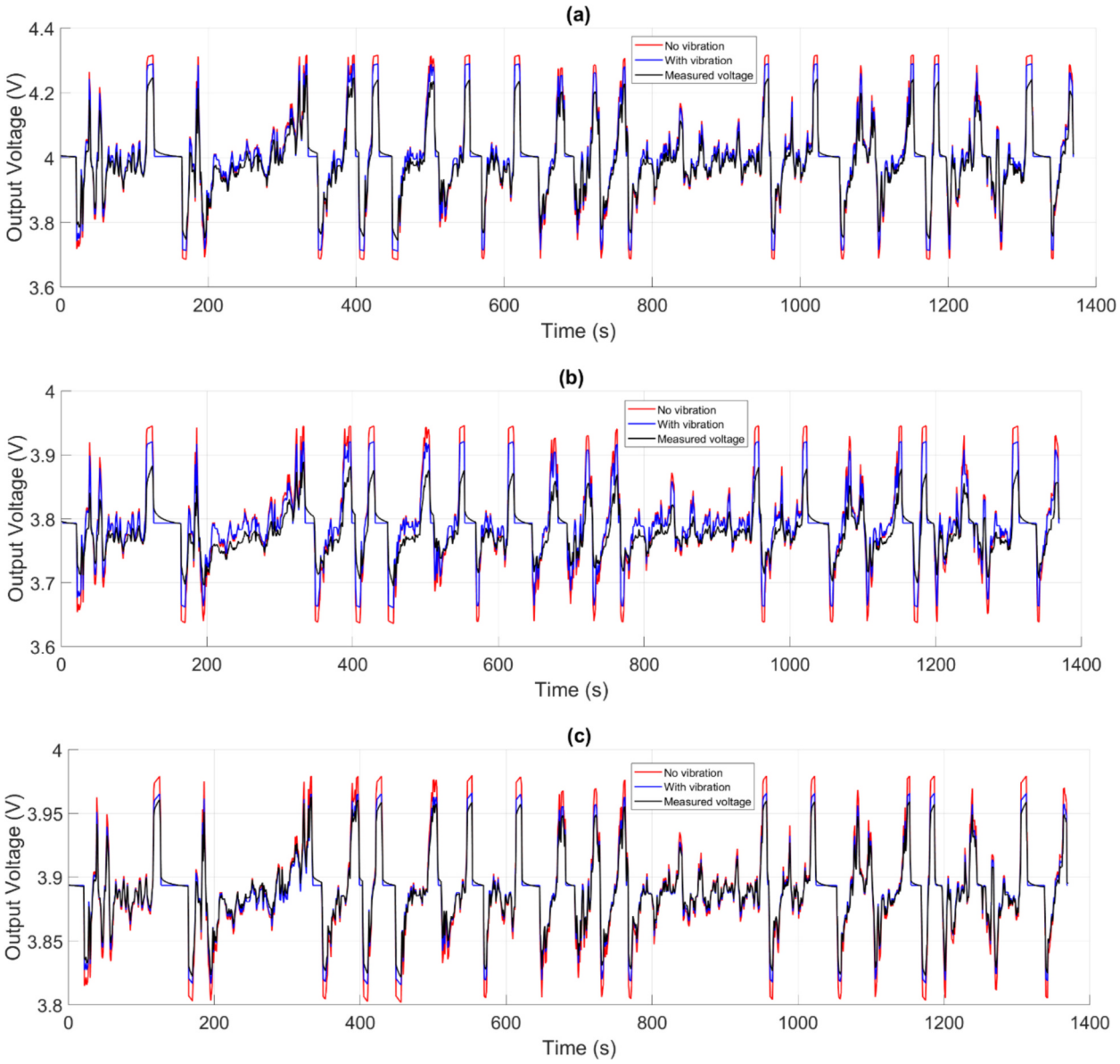


Fig. 21. Voltage output comparison between the experimental cell and the ECM considering without and with vibration influence. (a) at 10 °C and 85% SOC. (b) at 25 °C and 65% SOC. (c) at 35 °C and 75% SOC.

increased resistance across the board, particularly under high SOC and low-temperature conditions. These increases in resistance may be associated with mechanical degradation mechanisms reported in the literature [30,48], such as electrode cracking, contact loss, and active material detachment induced by vibrational stress. Although these effects were not directly characterised in this study, the observed electrochemical responses are consistent with such degradation pathways. However, it was also noticed that vibrations could reduce the resistance and capacitance at lower SOC, in particular, values below 10% SOC.

The ECM developed in this study was validated against a dynamic driving conditions cycle profile given by UDDS. The ECM demonstrates strong accuracy against the experimental results with an RMSE of 14 mV. Excluding the effects of vibrations increases the RMSE by 26%, showing the importance of accounting for mechanical stresses in battery management systems.

While the model accurately captures electrochemical behaviour through resistance and capacitance variations, it remains phenomenological in nature. The physical mechanisms underlying the observed resistance increases attributed to vibrations have not been directly verified. Future studies will aim to complement the electrochemical modelling with structural characterisation techniques, such as X-ray tomography or electron microscopy, to directly investigate material degradation pathways and enhance the physical interpretability of the ECM.

CRediT authorship contribution statement

Oscar E. Rojas: Writing – original draft, Investigation, Formal analysis, Data curation. **Ruben Hrstka-Sanchez:** Visualization, Methodology, Investigation. **Feiyang He:** Writing – review & editing, Writing – original draft, Validation, Methodology, Investigation, Formal analysis, Data curation. **Muhammad A. Khan:** Writing – review & editing, Supervision, Resources, Project administration, Methodology, Investigation, Conceptualization.

Declaration of competing interest

The authors declare that they have no known competing financial interests or personal relationships that could have appeared to influence the work reported in this paper.

Data availability

Data will be made available on request.

References

[1] J. Warner, History of vehicle electrification, in: The Handbook of Lithium-ion Battery Pack Design, 2015, https://doi.org/10.1016/b978-0-12-801456-1.00002-6.

[2] J.B. Goodenough, K.S. Park, The Li-ion rechargeable battery: a perspective, J. Am. Chem. Soc. 135 (2013), https://doi.org/10.1021/ja3091438.

[3] G. Zubi, R. Dufo-López, M. Carvalho, G. Pasaoglu, The lithium-ion battery: state of the art and future perspectives, Renew. Sust. Energ. Rev. 89 (2018), https://doi.org/10.1016/j.rser.2018.03.002.

[4] J. Warner, Lithium-ion and other cell chemistries, in: The Handbook of Lithium-Ion Battery Pack Design, 2015, https://doi.org/10.1016/b978-0-12-801456-1.00007-5.

[5] A. Barai, K. Uddin, W.D. Widanage, A. McGordon, P. Jennings, A study of the influence of measurement timescale on internal resistance characterisation methodologies for lithium-ion cells, Sci. Rep. 8 (2018), https://doi.org/10.1038/s41598-017-18424-5.

[6] W. Waag, S. Käbitz, D.U. Sauer, Experimental investigation of the lithium-ion battery impedance characteristic at various conditions and aging states and its influence on the application, Appl. Energy 102 (2013), https://doi.org/10.1016/j.apenergy.2012.09.030.

[7] M. Mathew, S. Janhunen, M. Rashid, F. Long, M. Fowler, Comparative analysis of lithium-ion battery resistance estimation techniques for battery management systems, Energies (Basel) 11 (2018), https://doi.org/10.3390/en11061490.

[8] S. Rodrigucs, N. Munichandraiah, A.K. Shukla, AC impedance and state-of-charge analysis of a sealed lithium-ion rechargeable battery, J. Solid State Electrochem. 3 (1999), https://doi.org/10.1007/s100080050173.

[9] T. Momma, M. Matsunaga, D. Mukoyama, T. Osaka, Ac impedance analysis of lithium ion battery under temperature control, J. Power Sources 216 (2012), https://doi.org/10.1016/j.jpowsour.2012.05.095.

[10] S. Ma, M. Jiang, P. Tao, C. Song, J. Wu, J. Wang, T. Deng, W. Shang, Temperature effect and thermal impact in lithium-ion batteries: a review, Prog. Nat. Sci. Mater. Int. 28 (2018), https://doi.org/10.1016/j.pnsc.2018.11.002.

[11] Y. Yue, S. Li, X. Cheng, J. Wei, F. Zeng, X. Zhou, J. Yang, Effects of temperature on the ohmic internal resistance and energy loss of Lithium-ion batteries under millisecond pulse discharge, J. Phys. Conf. Ser. (2022), https://doi.org/10.1088/1742-6596/2301/1/012014.

[12] S.H. Ahmed, X. Kang, S.O.B. Shrestha, Effects of temperature on internal resistances of lithium-ion batteries, J. Energy Resour. Technol. 137 (2015), https://doi.org/10.1115/1.4028698.

[13] F. Leng, C.M. Tan, M. Pecht, Effect of temperature on the aging rate of Li ion battery operating above room temperature, Sci. Rep. 5 (2015), https://doi.org/10.1038/srep12967.

[14] S. Seki, N. Kihira, Y. Mita, T. Kobayashi, K. Takei, T. Ikeya, H. Miyashiro, N. Terada, AC impedance study of high-power lithium-ion secondary batteries—effect of battery size, J. Electrochem. Soc. 158 (2011), https://doi.org/10.1149/1.3525277.

[15] A. Kumar, N.K. Roy, Study and modeling of internal resistance of Li-Ion battery with change in temperature & SoC, in: Proceedings - 2022 International Conference on Smart and Sustainable Technologies in Energy and Power Sectors, SSTEPS 2022, 2022, https://doi.org/10.1109/SSTEPS57475.2022.00024.

[16] M. Koseoglou, E. Tsioumas, I. Panagiotidis, D. Papagiannis, N. Jabbour, C. Mademlis, A lithium-ion battery equivalent circuit model based on a hybrid parametrization approach, J. Energy Storage 73 (2023), https://doi.org/10.1016/j.est.2023.109051.

[17] W. Waag, C. Fleischer, D.U. Sauer, On-line estimation of lithium-ion battery impedance parameters using a novel varied-parameters approach, J. Power Sources 237 (2013), https://doi.org/10.1016/j.jpowsour.2013.03.034.

[18] X. Hua, A. Thomas, Effect of dynamic loads and vibrations on lithium-ion batteries, J. Low Freq. Noise Vib. Act. Control 40 (2021), https://doi.org/10.1177/14613484211008112.

[19] P. Berg, M. Spielbauer, M. Tillinger, M. Merkel, M. Schoenfuss, O. Bohlen, A. Jossen, Durability of lithium-ion 18650 cells under random vibration load with respect to the inner cell design, J. Energy Storage 31 (2020) 101499, https://doi.org/10.1016/J.EST.2020.101499.

[20] P.Y. Lee, S. Park, I. Cho, J. Kim, Vibration-based degradation effect in rechargeable lithium ion batteries having different cathode materials for railway vehicle application, Eng. Fail. Anal. 124 (2021), https://doi.org/10.1016/j.engfailanal.2021.105334.

[21] J.M. Hooper, J. Marco, G.H. Chouchelamane, J.S. Chevalier, D. Williams, Multi-axis vibration durability testing of lithium ion 18650 NCA cylindrical cells, J. Energy Storage 15 (2018), https://doi.org/10.1016/j.est.2017.11.006.

[22] L. Somerville, J.M. Hooper, J. Marco, A. McGordon, C. Lyness, M. Walker, P. Jennings, Impact of vibration on the surface film of lithium-ion cells, Energies (Basel) 10 (2017), https://doi.org/10.3390/en10060741.

[23] J. Warner, Battery management system controls, in: The Handbook of Lithium-Ion Battery Pack Design, Elsevier, 2015, pp. 91–101, https://doi.org/10.1016/b978-0-12-801456-1.00008-7.

[24] M.K. Tran, M. Mathew, S. Janhunen, S. Panchal, K. Raahemifar, R. Fraser, M. Fowler, A comprehensive equivalent circuit model for lithium-ion batteries, incorporating the effects of state of health, state of charge, and temperature on model parameters, J. Energy Storage 43 (2021), https://doi.org/10.1016/j.est.2021.103252.

[25] G.L. Plett, Extended Kalman filtering for battery management systems of LiPB-based HEV battery packs - part 3. State and parameter estimation, J. Power Sources 134 (2004) 277–292, https://doi.org/10.1016/j.jpowsour.2004.02.033.

[26] D. Gandolfo, A. Brandão, D. Patiño, M. Molina, Dynamic model of lithium polymer battery - load resistor method for electric parameters identification, J. Energy Inst. 88 (2015), https://doi.org/10.1016/j.joei.2014.10.004.

[27] B. Bairwa, K. Pareek, K.A. Manohar, E. Nanditha Varshini, Electrical equivalent circuit modeling of lithium-ion battery, in: Proceedings of the 3rd International Conference on Smart Technologies in Computing, Electrical and Electronics, ICSTCEE 2022, 2022, https://doi.org/10.1109/ICSTCEE56972.2022.10100238.

[28] Z. Gao, C.S. Chin, W.L. Woo, J. Jia, Integrated equivalent circuit and thermal model for simulation of temperature-dependent LiFePO4 battery in actual embedded application, Energies (Basel) 10 (2017), https://doi.org/10.3390/en10010085.

[29] O.E. Rojas, M.A. Khan, Performance and Safety Evaluation of lithium-Ion Batteries for Electric Vehicles. https://ssrn.com/abstract=3945961, 2021.

[30] O.E. Rojas, M.A. Khan, A review on electrical and mechanical performance parameters in lithium-ion battery packs, J. Clean. Prod. 378 (2022), https://doi.org/10.1016/j.jclepro.2022.134381.

[31] NCR18650 20R, (n.d.).

[32] G. Kjell, J.F. Lang, Comparing different vibration tests proposed for Li-ion batteries with vibration measurement in an electric vehicle, in: 2013 World Electric Vehicle Symposium and Exhibition, EVS 2014, 2014, https://doi.org/10.1109/EVS.2013.6914869.

[33] ISO12405-1, Electrically propelled road vehicles - test specification for lithium-ion traction battery packs and systems - part 1: high-power applications, Ergonomics 2000 (2002).

[34] Y. Chen, K. Mitsubori, Dependence of OCV, Hysteresis, Overvoltage on Temperature and SOC in Commercial LiFePO4 Lithium-Ion Battery. Electronics Letters, Electron. Lett. 61 (1) (2025) e70403, https://doi.org/10.1049/ell2.70403.

[35] W. Waag, S. Käbitz, D.U. Sauer, Experimental investigation of the lithium-ion battery impedance characteristic at various conditions and aging states and its influence on the application, Appl. Energy 102 (2013) 885–897, https://doi.org/10.1016/j.apenergy.2012.09.030.

[36] J. Sun, J. Kainz, Optimization of hybrid pulse power characterization profile for equivalent circuit model parameter identification of Li-ion battery based on Taguchi method, J. Energy Storage 70 (2023) 108034.

[37] F. Zheng, Y. Xing, J. Jiang, B. Sun, J. Kim, M. Pecht, Influence of different open circuit voltage tests on state of charge online estimation for lithium-ion batteries, Appl. Energy 183 (2016), https://doi.org/10.1016/j.apenergy.2016.09.010.

[38] Y. Ko, W. Choi, A new soc estimation for lfp batteries: application in a 10 ah cell (hw 38120 l/s) as a hysteresis case study, Electronics (Switzerland) 10 (2021), https://doi.org/10.3390/electronics10060705.

[39] Z. Liu, C. Wang, X. Guo, S. Cheng, Y. Gao, R. Wang, Y. Sun, P. Yan, Thermal characteristics of ultrahigh power density lithium-ion battery, J. Power Sources 506 (2021), https://doi.org/10.1016/j.jpowsour.2021.230205.

[40] Q. Zhang, C.G. Huang, H. Li, G. Feng, W. Peng, Electrochemical impedance spectroscopy based state-of-health estimation for lithium-ion battery considering temperature and state-of-charge effect, IEEE Trans. Transp. Electrific. 8 (2022), https://doi.org/10.1109/TTE.2022.3160021.

[41] P. Singh, R. Vinjamuri, X. Wang, D. Reisner, Fuzzy logic modeling of EIS measurements on lithium-ion batteries, Electrochim. Acta (2006), https://doi.org/10.1016/j.electacta.2005.02.143.

[42] U. Westerhoff, K. Kurbach, F. Lienesch, M. Kurrat, Analysis of lithium-ion battery models based on electrochemical impedance spectroscopy, Energ. Technol. 4 (2016), https://doi.org/10.1002/ente.201600154.

[43] T.F. Su, K.C. Chen, Rapid monitor of states of lithium-ion batteries through non-quasi-static electrochemical impedance spectroscopy and terminal voltage, J. Power Sources 586 (2023), https://doi.org/10.1016/j.jpowsour.2023.233641.

[44] J. Li, E. Murphy, J. Winnick, P.A. Kohl, Studies on the cycle life of commercial lithium ion batteries during rapid charge-discharge cycling, J. Power Sources 102 (2001), https://doi.org/10.1016/S0378-7753(01)00821-7.

[45] F. Feng, R. Yang, J. Meng, Y. Xie, Z. Zhang, Y. Chai, L. Mou, Electrochemical impedance characteristics at various conditions for commercial solid–liquid electrolyte lithium-ion batteries: part 1. Experiment investigation and regression analysis, Energy 242 (2022), https://doi.org/10.1016/j.energy.2021.122880.

[46] S. Potrykus, F. Kutt, J. Nieznanski, F.J.F. Morales, Advanced lithium-ion battery model for power system performance analysis, Energies (Basel) 13 (2020), https://doi.org/10.3390/en13102411.

[47] B. Sungur, A. Kaleli, State of charge estimation for lithium-ion batteries using optimized model based on optimal HPPC conditions created using Taguchi method and multi-objective optimization, Appl. Sci. 14 (2024) 9245, https://doi.org/10.3390/APP14209245.

[48] A. Mukhopadhyay, B.W. Sheldon, Deformation and stress in electrode materials for Li-ion batteries, Prog. Mater. Sci. 63 (2014), https://doi.org/10.1016/j.pmatsci.2014.02.001.
[49] M. Dubarry, A. Devie, B.Y. Liaw, The value of battery diagnostics and prognostics, J. Energy Power Sources 1 (2014).
[50] Y. Li, L. Zhou, H. Jiang, Q. Zhang, S. Zhang, X.Ming Zhu H., Vibration induced performance degradation on $LiNi_{0.5}Co_{0.2}Mn_{0.3}O_2$/graphite lithium-ion battery, J. Energy Storage (2025), https://doi.org/10.1016/j.est.2025.117700.
[51] H.G. Kim, G.C. Kim, W. Ji, Y.S. Lee, S. Jang, C.M. Shin, Random vibration fatigue analysis of a multi-material battery pack structure for an electric vehicle, Funct. Compos. Struct. 3 (2021), https://doi.org/10.1088/2631-6331/ac0416.
[52] B. Plaumann, Towards realistic vibration testing of large floor batteries for battery electric vehicles (BEV), Sound Vib. 56 (2022), https://doi.org/10.32604/SV.2022.018634.
[53] L. Shui, F. Chen, A. Garg, X. Peng, N. Bao, J. Zhang, Design optimization of battery pack enclosure for electric vehicle, Struct. Multidiscip. Optim. 58 (2018), https://doi.org/10.1007/s00158-018-1901-y.
[54] R. Li, F. He, O.R. Vargas, M. Khan, Capacity and impedance characteristics of the lithium-ion battery and mechanical properties of the battery pack under coupled temperature-vibration conditions: an experimental approach, J. Power Sources 652 (2025) 237688, https://doi.org/10.1016/J.JPOWSOUR.2025.237688.
[55] S. Barcellona, S. Colnago, L. Codecasa, L. Piegari, Unified model of lithium-ion battery and electrochemical storage system, J. Energy Storage 73 (2023), https://doi.org/10.1016/j.est.2023.109202.



https://dspace.org/

Equivalent circuit model for electrical performance characterisation of lithium-ion batteries under thermo-mechanical loads

Rojas, Oscar E.; Hrstka-Sanchez, Ruben; He, Feiyang; Khan, Muhammad A.

2026-05-01
Elsevier
https://doi.org/10.1016/j.est.2026.121636
Rojas OE, Hrstka-Sanchez R, He F, Khan MA. (2026) Equivalent circuit model for electrical performance characterisation of lithium-ion batteries under thermo-mechanical loads. Journal of Energy Storage, Volume 157, May 2026, Article number 121636

Downloaded from a DSpace repository. https://dspace.org/